11-26-2019

Crystallization-Driven Self-Assembly of Coil-Comb-Shaped Polypeptoid Block Copolymers: Solution Morphology and Self-Assembly Pathways

Naisheng Jiang
Louisiana State University

Tianyi Yu
Louisiana State University

Omead A. Darvish
Louisiana State University

Shuo Qian
Oak Ridge National Laboratory

Igor Kevin Mkam Tsengam
Tulane University

See next page for additional authors

Recommended Citation

Jiang, N., Yu, T., Darvish, O., Qian, S., Mkam Tsengam, I., John, V., & Zhang, D. (2019). Crystallization-Driven Self-Assembly of Coil-Comb-Shaped Polypeptoid Block Copolymers: Solution Morphology and Self-Assembly Pathways. *Macromolecules, 52* (22), 8867-8877. https://doi.org/10.1021/acs.macromol.9b01546

Crystallization-Driven Self-Assembly of Coil-Comb Shaped Polypeptoid Block Copolymers: Solution Morphology and Self-Assembly Pathways

Naisheng Jiang,[1, ±*] *Tianyi Yu,*[1] *Omead A. Darvish,*[1] *Shuo Qian,*[2] *Igor Kevin Mkam Tsengam,*[3] *Vijay John,*[3] *and Donghui Zhang*[1*]

[1]Department of Chemistry, Louisiana State University, Baton Rouge, Louisiana 70803, United States

[2] Neutron Scattering Division, Oak Ridge National Laboratory, Oak Ridge, Tennessee 37830, United States

[3]Department of Chemical and Biomolecular Engineering, Tulane University, New Orleans, Louisiana 70118, United States

[±]Present Address: School of Materials Science and Engineering, University of Science and Technology Beijing, Beijing 100083, China

Corresponding to: dhzhang@lsu.edu, naishengjiang@gmail.com

ABSTRACT

Crystallization-driven self-assembly (CDSA) of amphiphilic polymers into well-defined nanoscopic structures with different morphologies and functionalities has attracted increasing attention. Here, we investigate the CDSA of coil-comb shaped diblock copolypeptoids, namely poly(*N*-methyl glycine)-*b*-poly(*N*-decyl glycine) (PNMG-*b*-PNDG), in dilute methanol solution using X-ray/neutron solution scattering in conjunction with cryogenic transmission electron microscopy (cryo-TEM) techniques. A series of PNMG-*b*-PNDGs were synthesized by sequential benzyl amine-initiated ring-opening polymerizations of the corresponding *N*-substituted *N*-carboxyanhydrides, in which the degree of polymerization and the length of the blocks were varied. The PNMG-*b*-PNDG polymers with lower volume fraction of the crystalline PNDG blocks (f_{PNDG} = 0.44) were found to slowly self-assemble into one-dimensional long worm-like nanofibrils in methanol. The nanofibrils bear anisotropic crystalline core where the comb-shaped PNDG blocks were stacked in a face-to-face fashion along the long axis of the nanofibrils. Upon increasing f_{PNDG} to 0.61 and 0.68, the final morphology of PNMG-*b*-PNDG micelles changed from worm-like nanofibrils to rigid short nanorods and then two-dimensional nanosheets. The nanofibrils were formed by a self-seeding growth pathway that involves the initial formation of a few seeded crystals followed by the addition of soluble unimers to the preferred crystal facets resulting in the gradual elongation of the micelles. By contrast, the nanorods were formed by a two-stage process involving the formation of spherical micelles with an amorphous core in the first stage and rapid confined crystallization of the micellar core and their fusion into the rod-like nanostructures at the second stage. Understanding the relationship between chemical composition, micellar morphology and CDSA pathway of coil-comb shaped diblock copolypeptoids

is an important step towards the rational design of anisotropic polymeric nanostructures with tailorable morphology.

INTRODUCTION

Anisotropic polymeric nanostructures such as one-dimensional (1D) nanorods, nanoribbons two-dimensional (2D) nanosheets or platelets) have attracted growing interests due to their potential for biomedical and biotechnological applications (*e.g.*, drug delivery[1, 2] and biomineralization).[3] Crystallization-driven self-assembly (CDSA)[4-6] of coil-crystalline block copolymers (BCPs) has been demonstrated as an effective strategy to access anisotropic polymeric nanostructures. AB-type diblock copolymers comprised of solvophilic corona-forming segments and crystallizable core-forming segments are the most commonly used structural motif to induce the formation of anisotropic nanostructures in solution by the CDSA process.[7] A number of well-known polymers that can crystallize by the chain folding mechanism (*e.g.*, polyethylene,[8, 9] polyethylene oxide,[10] poly(ε-caprolactone)[11-13] and polylactide)[14-17] have been investigated as crystalline core-forming segments. Metallopolymers (*e.g.*, polyferrocenylsilanes)[18-26] and π-conjugated polymers with more rigid backbones (*e.g.*, poly(3-alkylthiophenes))[7, 27-31] have also served as crystalline core-forming blocks to facilitate the formation of a variety of nanostructures by CDSA for targeted applications.

The morphology of nanostructures obtained by CDSA strongly depends on the specific polymer composition[16, 21] and the self-assembly pathway.[9, 32] With these solvophobic crystalline blocks, the molecular exchange is often restricted due to high free energy penalty, resulting in kinetically trapped molecular assemblies in an out-of-equilibrium state with a very long lifetime.[5, 8, 32-35] As a result, one can access anisotropic polymeric nanostructures with varying morphology by altering the solvent,[9, 11, 15, 20, 22] length of the solvophobic crystallizable block[16, 17] and annealing condition.[20] In some cases, CDSA of block copolymers can proceed in a living fashion in solution, allowing access to sophisticated hierarchical nanostructures with tailorable shape, size and low polydispersity.[4, 7, 14, 19, 20, 23-28]

Polypeptoids featuring *N*-substituted polyglycine backbones are structural mimics of polypeptides.[36-39] In contrast to polypeptides, polypeptoids exhibit thermal processability, enhanced protease stability and good solubility in water and common organic solvents due to the absence of hydrogen bonding and stereogenic centers along the backbone, in sharp contrast to polypeptides. The cytocompatibility and biodegradability also make polypeptoids an attractive class of biomimetic polymers for biomedical and biotechnological applications (*e.g.*, antifouling coatings, drug/gene delivery and biosensor).[39-42] Recent developments in the controlled polymerization and solid-phase synthesis have enabled access to a variety of polypeptoids with tailorable chain length, microstructure and architecture, setting the stage for the further investigation of their solution and solid-state self-assembly behaviors.[43-54] It has been found that polypeptoids with relatively short *n*-alkyl side-chains ($n \leq 2$), such as poly(*N*-methyl glycine) (PNMG) (*a.k.a.* polysarcosine), are amorphous with random-coil conformations similar to conventional amorphous polymers.[36, 55] By contrast, comb-shaped polypeptoids with relatively long *n*-alkyl side chains ($4 \leq S \leq 14$, where S is the number of carbon atoms in the linear *n*-alkyl group) are crystallizable and exhibit two phase transitions with the temperature change, *i.e.*, a crystalline phase and a "sanidic" liquid crystalline (LC) mesophase, prior to isotropic melting.[46, 50] It should be noted that crystallization of these comb-shaped polypeptoids can occur at relatively low degree of polymerization (>10 mer).[56, 57] In the crystalline phase, the polypeptoids chain adopt a board-like structure where the backbone is fully extended in an all *cis*-amide conformation and is approximately coplanar with the *n*-alkyl side chains (Figure S1).[50, 51] Here, the intermolecular interactions between *n*-alkyl side chains are likely arise from van der Waals interactions (or packing constraints in the crystalline lattice), whereas the interactions between all *cis*-amide backbones may involve additional contributions, such as CH···O hydrogen bonding or amide

dipole interactions.[50, 51, 58] The all *cis*-amide backbone conformation, which is more compact and possesses a higher degree of ordering than the all *trans*-amide conformation, allows for more favorable intra- and inter-molecular interactions during self-assembly processes.[51, 58] Considering the unique crystalline packing of polypeptoids, we reason that amphiphilic diblock copolypeptoids comprised of a comb-shaped crystallizable segment and a coil-like amorphous segment are well-suited to generate fully biocompatible and biodegradable polymeric nanostructures with high aspect ratios in solution by the CDSA process. We previously showed that diblock copolypeptoids (*i.e.*, $PNMG_{112}$-*b*-$PNDG_{16}$) comprised of a soluble coil-like PNMG block and a crystallizable comb-like poly(*N*-decyl glycine) (PNDG) block slowly self-assembled into long, worm-like nanofibrils in dilute methanol via CDSA.[44] With similar coil-comb shaped polypeptoid-based diblock copolymers, *i.e.*, poly(ethylene glycol)-*b*-poly(*N*-octyl glycine), Sun, Li and coworkers reported the formation of 2D nanosheets through a sphere-to-cylinder-to-nanosheet transition pathway during CDSA in dilute ethanol.[52] Using a cosolvent strategy, they also demonstrated the hierarchical self-assembly of 2D nanosheets induced by the fusion of early nanofibrils comprised of coil-crystalline poly(ethylene glycol)-*b*-poly(*N*-(2-phenylethyl) glycine).[53] Interestingly, instead of forming a core-shell type nanostructure, Zuckermann and coworkers reported that comb-comb shaped diblock copolypeptoids, *i.e.*, poly(*N*-2-(2-(2-methoxyethoxy)ethoxy)ethyl glycine)-*b*-poly(*N*-decyl glycine), self-assemble into hollow, multiwalled nanotubes in water via the co-crystallization of both hydrophilic and hydrophobic blocks.[49] In spite of the increasing reports on polypeptoid-based nanostructures generated by CDSA, the molecular arrangement at the nanometer scale and the underlying self-assembly mechanism of these nanostructures are not well understood.

In this contribution, we report a study on the CDSA of coil-comb shaped diblock copolypeptoids,

namely poly(*N*-methyl glycine)-*b*-poly(*N*-decyl glycine) (PNMG-*b*-PNDG), in dilute methanol solution by a combination of X-ray/neutron scattering and cryogenic transmission-electron microscopic (cryo-TEM) techniques. The shape, size and molecular packing of the self-assembled PNMG-*b*-PNDG nanostructures have been found to depend strongly on the relative volume fraction and chain length of PNDG segments. As the volume fraction and the chain length of PNDG block increases, the morphology of self-assembled nanostructures changes from 1D worm-like nanofibrils, to 1D short nanorods and then to 2D nanosheets. The nanofibrils were shown to form by a self-seeding growth mechanism with the comb-like PNDG blocks stacked in a face-to-face fashion along the long axis of nanofibrils, resulting in anisotropic crystalline cores. By contrast, the formation of nanorods occurred by a two-stage process, involving the initial formation of spherical micelles followed by rapid confined crystallization of micellar cores and fusion into rod-like nanostructures. These findings on the molecular arrangement and the formation mechanism of PNMG-*b*-PNDG nanostructures in dilute solution not only provide a new strategy towards the rational design of polypeptoid-based nanostructures with tunable size, shape and morphology, but also shed lights on the CDSA of comb-shaped polymers bearing long and linear aliphatic side chains in general.

RESULTS AND DISCUSSION

Polymer Composition and Preparation of Micellar Solution. A series of linear amphiphilic diblock copolypeptoids, *i.e.* poly(*N*-methyl glycine)-*b*-poly(*N*-decyl glycine) (PNMG-*b*-PNDG), with different number-average degree of polymerization and volume fraction of the PNDG segment have been synthesized by the benzyl amine-initiated ring-opening polymerization of the corresponding *N*-substituted *N*-carboxyanhydrides (R-NCAs) in a sequential manner (Scheme S1).[43-45, 48] The polymer composition of PNMG-*b*-PNDG samples has been determined by ^{1}H NMR spectroscopic analysis

(Figure S2-S4) and summarized in Table 1. Size-exclusion chromatography (SEC) analysis of the polymers revealed monomodal molecular weight distribution with polydispersity index (PDI) in the 1.07-1.26 range (Figure S5). As the PNMG block is solvophilic and the PNDG block is relatively solvophobic in methanol, as indicated by the liquid contact-angle measurements (Figure S6), PNMG-*b*-PNDG block copolymers with varying composition are expected to form intermolecular assemblies in methanol. We have found that all diblock copolypeptoids can be readily dissolved at a 5 mg/ml concentration in methanol with heating at ~ 65 °C for 1 h. No sign of crystallization of PNDG blocks was observed at 65 °C in the polymer solution, evidenced by the high temperature SAXS/WAXS measurements (*vide infra*). Crystallization of PNDG blocks occurred upon cooling the PNMG-*b*-PNDG solution from 65°C to room temperature,[44, 45] facilitating the crystallization-driven self-assembly (CDSA) of diblock copolypeptoids in methanol. The solutions were left at room temperature for at least 15 days prior to further structural characterization by a combination of transmission-electron microscopy and neutron/X-ray scattering methods. (Note: previous studies have shown that 15 days is sufficient for the formation of self-assembled PNMG-*b*-PNDG nanostructures in 5 mg/mL methanol solution).[44]

Table 1. Molecular characteristics of PNMG-*b*-PNDG diblock copolymers and structural parameters of PNMG-*b*-PNDG nanostructures obtained by CDSA

Composition of PNMG-*b*-PNDG	f_{PNDG} [a]	Micellar Morphology	R_c [b] (nm)	$R_{g,chain}$ [c] (nm)	σ_R [d]	$N_{agg,\ cross}$ [e]	$d_{(001)}$ [f] (nm)	$d_{(100)}$ [g] (nm)	Diameter (SANS)[h] (nm)	Diameter (cryo-TEM)[i] (nm)
$PNMG_{105}$-*b*-$PNDG_{20}$	0.44	Nanofibrils	3.3± 0.2	3.8± 0.2	0.4	~2	2.4	0.46	~23.4	~20
$PNMG_{121}$-*b*-$PNDG_{46}$	0.61	Nanorods	6.8± 0.2	5.8± 0.2	0.3	~4	2.4	0.46	~38.0	~27
$PNMG_{124}$-*b*-$PNDG_{63}$	0.68	Nanosheets	N/A	N/A	N/A	N/A	2.5	N/A	N/A	N/A

[a.] The volume fraction of PNDG block (f_{PNDG}) was calculated from the block copolymer composition and the density for each block. [b.] R_c is the core cross-sectional radius. [c.] $R_{g,\ chain}$ is the radius of gyration for the corona chain. [d.] The polydispersity values of core cross-section radius (σ_R) were obtained from the SANS analysis. The corresponding R_c distributions of $PNMG_{105}$-*b*-$PNDG_{20}$ nanofibrils and $PNMG_{121}$-*b*-$PNDG_{46}$ nanorods were shown in Figure S8. [e.] The lower bound values of average number of polymer chains in the cross-sectional area ($N_{agg,\ cross}$) were estimated using the equation $N_{agg,\ cross} \approx \pi R_c^2/(l_b l_c)$, where l_b and l_c correspond to the dimensions of fully extended PNDG segments along the crystallographic b and c axis, respectively. [f.] *d*-spacing of the (001) packing of the PNDG crystalline domain ($d_{(001)}$) was determined by MAXS. [g.] *d*-spacing of the (100) packing of the PNDG crystalline domain ($d_{(100)}$) was determined by WAXS. [h.] The average diameter of the 1D nanostructures obtained from SANS model fitting. [i.] The average diameter of the 1D nanostructures obtained from cryo-TEM imaging.

Structural Elucidation of Coil-Comb Shaped Diblock Copolypeptoid Micelles. Cryo-TEM analysis of the vitrified $PNMG_{105}$-*b*-$PNDG_{20}$ methanol solution (1 mg/mL obtained by dilution from 5 mg/mL solution) (Figure 1(a)) has revealed the formation of micron long worm-like nanofibrils with

an average diameter of ~ 20 nm. It was also found that the overall morphology for PNMG$_{105}$-*b*-PNDG$_{20}$ nanostructures remains nearly identical in a broad concentration range (2.7 - 25 mg/mL) (Figure S7). To obtain detailed structural information of the nanofibrils, we conducted small-angle neutron scattering (SANS) and small angle X-ray scattering (SAXS) experiments on the 5 mg/mL PNMG$_{105}$-*b*-PNDG$_{20}$ methanol solution. Figure 1(b) shows the SANS profile of the 5 mg/mL PNMG$_{105}$-*b*-PNDG$_{20}$ methanol solution measured at room temperature using a quartz "banjo" cell. At the low q regime (q < 0.005 Å^{-1}), the scattering intensity exhibits a power-law dependence on q (*i.e.*, I ~ $q^{-\alpha}$) with an exponent (α) of -1, indicating the formation of one-dimensional elongated rod-like nanostructures in methanol. Based on the SANS and cryo-TEM results, it is reasonable that the PNMG$_{105}$-*b*-PNDG$_{20}$ molecules can self-assemble into elongated rod-like micelles comprised of a collapsed PNDG core and a shell with swollen PNMG chains.

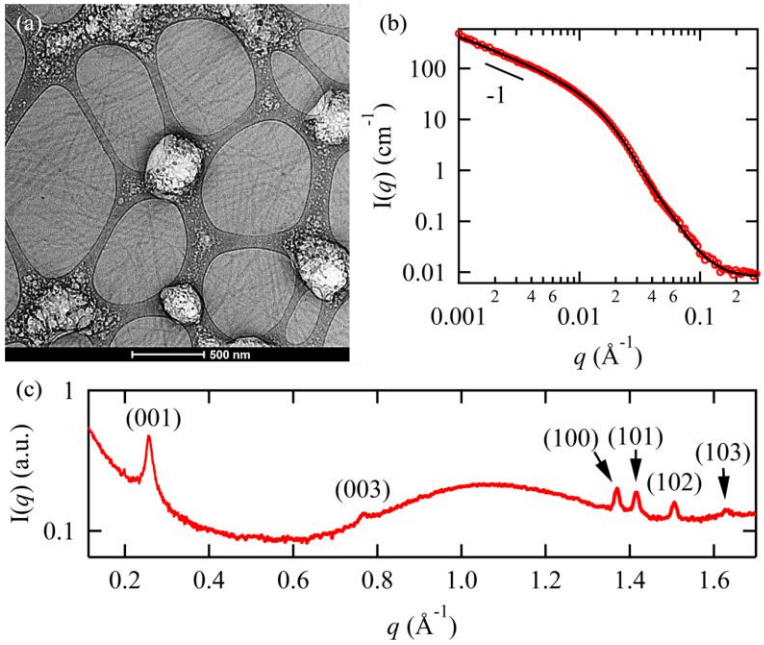

Figure 1. (a) Representative cryo-TEM image for PNMG$_{105}$-*b*-PNDG$_{20}$ in diluted methanol solution (1 mg/mL). (b) SANS intensity profile (open circles) for the 5 mg/ml PNMG$_{105}$-*b*-PNDG$_{20}$ in deuterated methanol measured at static state at room temperature. The solid line corresponds to the best-fit to the data based on the cylindrical micelle model described in the text. (c) MAXS/WAXS intensity profile for the 5 mg/ml PNMG$_{105}$-*b*-PNDG$_{20}$ in methanol measured at a static state at room temperature.

The scattering model for core-shell rod-like micelles (*a.k.a.* cylindrical micelles), which was initially developed by Pedersen and co-workers,[59, 60] has been used to fit the SANS intensity profiles

of the $PNMG_{105}$-*b*-$PNDG_{20}$ solution (Figure 1(b)). The detailed description of the scattering model was summarized in the SI. In brief, the scattering form factor of a single micelle with a compact rod-shaped core surrounded by Gaussian corona chains at the core surface consists of four different terms: the self-correlation of the rod-like core, the self-correlation of the chains, the cross term between the rod-like core and chains, and the cross term between different chains, which are expressed in terms of the core cross-sectional radius (R_c) and length (L_c), as well as the radius of gyration ($R_{g,\ chain}$) of the Gaussian corona chains that are centered at a distance $d_{int}R_{g,\ chain}$ away from the surface of the rod-like core (d_{int} is close to unity to mimic non-penetration of the corona chains into the core region). Dispersity in R_c was also included in the modeling by a lognormal distribution of core radii with a polydispersity σ_R. It should be mentioned that the rod-like micelle model assumes the core to have a circular cross-section. While it will be shown later that the PNDG segments crystallize in the micelles to form an anisotropic core which cannot have an exactly circular cross-section (*vide infra*), the good fitting of the SANS/SAXS data with the rod-like micelle model suggests the cross-section of the PNDG core can be approximated as a circular shape (Figure 1(b)).

In the fitting of SANS data, four independent parameters could be adjusted: the core radius (R_c), core length (L_c), the radius of gyration of the corona chains ($R_{g,\ chain}$), the polydispersity of core radius (σ_R). The d_{int} value is constrained within a range of 0.9 to 1 based on the previous study by Pedersen and Gerstenberg on the core-shell micelles.[59] The *SLD* values and molecular volume of PNDG (V_{core}) and PNMG (V_{corona}) were estimated based on the bulk densities of PNDG and PNMG homopolymers (0.95 g/cm^3 for PNDG[47, 49] and 1.405 g/cm^3 for PNMG[61]) and were kept invariant during fitting procedure. A constant term that represents the incoherent scattering background, which mainly due to the presence of hydrogen in the sample, was also included. Due to the limited *q* range in the scattering

experiments and possible polydispersity of the L_c, the value of L_c cannot be accurately determined from the present model fitting of the SANS data. However, the exponential decay of I(q) near q ~ 0.013 Å^{-1} still provides useful structural information regarding the cross-section of the long worm-like nanofibrils. From the best-fit to the data, the R_c was estimated to be 3.3 $\pm$ 0.2 nm with a polydispersity (σ_R) of 0.4 (Figure S8). The $R_{g,\ chain}$ value was estimated to be 3.8 $\pm$ 0.2 nm. The thickness of the corona (h_{corona}) is then calculated to be 8.4 $\pm$ 0.2 nm using the $h_{corona} = (d_{int} + 1.291)$ $R_{g,\ chain}$ relationship. Therefore, the average diameter of the PNMG$_{105}$-*b*-PNDG$_{20}$ cylinders by SANS analysis is approximately 23.4 nm, in good agreement with the cryo-TEM result (~ 20 nm) (Figure 1(a)). It should be noted that the SAXS data for the same sample (Figure 5(a), *vide infra*) can be well-fitted using the same scattering model with identical R_c and R_g values obtained from SANS, further supporting the validity of the fitting results.

Figure 1(c) shows the one-dimensional mid- and wide-angle X-ray scattering (M/WAXS) profile of the 5 mg/mL PNMG$_{105}$-*b*-PNDG$_{20}$ methanol solution, which was obtained simultaneously with the SAXS measurement. Note that the measurement was conducted at a static state (*i.e.* the solution was not subjected to flow), and the resultant two-dimensional SAXS, MAXS and WAXS images display isotropic ring-like scattering patterns (Figure S9). A sharp scattering peak was observed at q = 0.26 Å^{-1}, corresponding to a d-spacing of 2.4 nm by the $d = 2\pi/q$ relationship. This d-spacing corresponds to the distance between adjacent backbones of PNDG segments that are separated by the long *n*-decyl side chains in the board-like crystalline packing,[44-47, 49-51] *i.e.*, the (001) packing along the crystallographic c-axis, as illustrated in Figure S1. In addition, a higher order peak due to (003) packing is present at $3q$ = 0.78 Å^{-1}. The (002) peak, which is expected to be located near $2q$ = 0.52 Å^{-1}, is barely discernible. The more intense (003) peak compared to (002) indicates the formation of well-organized,

symmetric lamellar structure inside the micellar core. At higher q region, we observed the (100) reflection at q = 1.37 Å^{-1}, corresponding to the closest packing distance between PNDG backbones along the crystallographic a-axis of the board-like crystalline structure (Figure S1) with a d-spacing of 0.46 nm.[50, 51] Higher order reflections from (101), (102) and (103) planes are also present (Figure 1(c)), indicating the long-range structural correlation between the nearly mutually perpendicular a-axis and c-axis as expected in the board-like crystalline structure (Figure S1).[51] In addition to these sharp scattering peaks, a broad peak centered at q = 1.1 Å^{-1} is also visible. While we attribute this mainly to incomplete background subtraction of the SAXS data, it may arise from some amorphous domains in the nanofibrils.

It is clear that the structure of PNDG segments inside the crystalline domains of the nanofibril's core is consistent the reported board-like crystalline packing of polypeptoids where the backbones adopt all *cis*-amide conformation.[50, 51] A critical question thus arises: how are the crystalline domains of $PNDG_{20}$ arranged inside the nanofibrils? Are they randomly oriented to form an isotropic core or preferentially oriented in a certain direction to form an anisotropic core within the nanofibrils? It is well-known that elongated particles tend to re-orient themselves under shear so that the long axis of the particles becomes parallel with the flow direction when being passed through a confined space.[62-65] To gain additional insights regarding the orientational ordering of the crystalline domains within the nanofibril's core, we conducted S/M/WAXS experiments on the methanol solution containing $PNMG_{105}$-*b*-$PNDG_{20}$ nanofibrils under unidirectional flow in a capillary flow cell (with an inner diameter of 1.47 mm). The corresponding flow cell geometry is depicted in Figure S10 and details of the measurements were summarized in the Supporting Information. Figure 2 shows the two-dimensional (2D) SAXS, MAXS and WAXS data of the 5 mg/mL methanol solution containing the

PNMG$_{105}$-*b*-PNDG$_{20}$ nanofibrils measured at room temperature under continual unidirectional flow with a constant shear rate of ~ 25.6 s^{-1} near the capillary wall. A shear rate (or flow rate)-dependent anisotropy of the scattering patterns is evident (Figure S11). Under a shear rate of ~ 25.6 s^{-1} near the wall, the 2D SAXS pattern shows clear anisotropy of scattering intensity with lower intensity along the scattering vector in the flow direction ($q_{//}$) relative to that along the scattering vector perpendicular to the flow direction ($q_{\perp}$). The scattering pattern clearly indicates the partial alignment of the long axis of PNMG$_{105}$-*b*-PNDG$_{20}$ nanofibrils parallel to the flow direction.[62-65] Meanwhile, M/WAXS analysis has revealed a significantly more pronounced scattering peak due to the (001) reflection in the $q_{\perp}$ direction relative to that in the $q_{//}$ direction, indicating that the (001) molecular packing separated by the *n*-decyl side chains with a *d*-spacing of d_{001} = 2.4 nm was aligned in the direction perpendicular to the long axis of the PNMG$_{105}$-*b*-PNDG$_{20}$ nanofibrils. Consistently, the scattering peaks due to (100) reflection and the associated higher order reflections from (101) and (102) planes are more notable along the $q_{//}$ direction as compared to those in the $q_{\perp}$ direction. This indicates

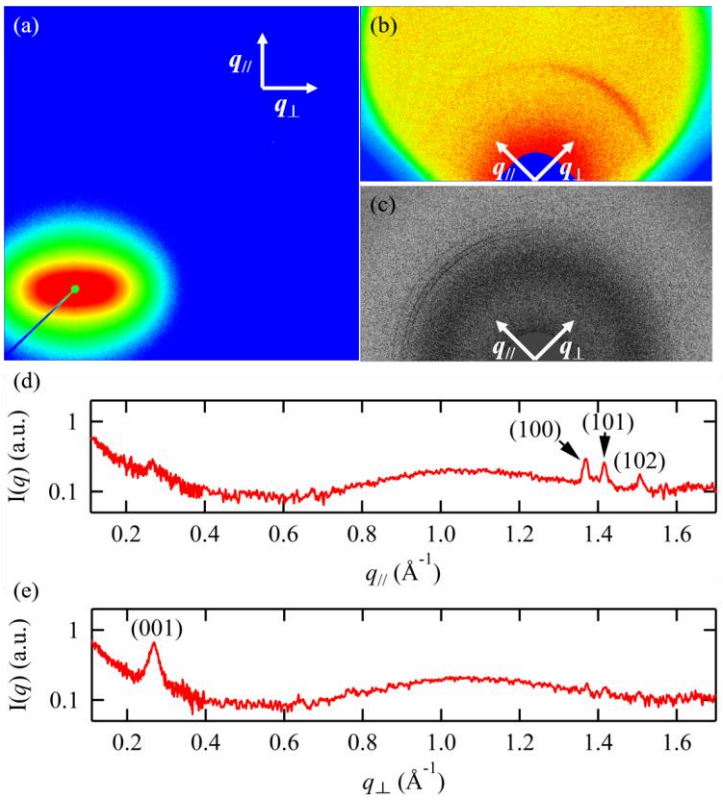

Figure 2. Two-dimensional (a) SAXS, (b) MAXS and (c) WAXS images for 5 mg/ml PNMG$_{105}$-*b*-PNDG$_{20}$ in diluted methanol solution measured during unidirectional flow at room temperature. The directions parallel ($q_{//}$) and perpendicular ($q_{\perp}$) to the flow direction are indicated by arrows. The corresponding one-dimensional profiles of the MAXS/WAXS results along the $q_{//}$ and $q_{\perp}$ directions are plotted in (d) and (e), respectively.

that the adjacent *cis*-amide backbones with a *d*-spacing of d_{100} = 0.46 nm was aligned in a direction parallel to the long axis of the nanofibrils. These combined results support an anisotropic crystalline core structure for the PNMG$_{105}$-*b*-PNDG$_{20}$ nanofibrils, as depicted in Figure 3(a).

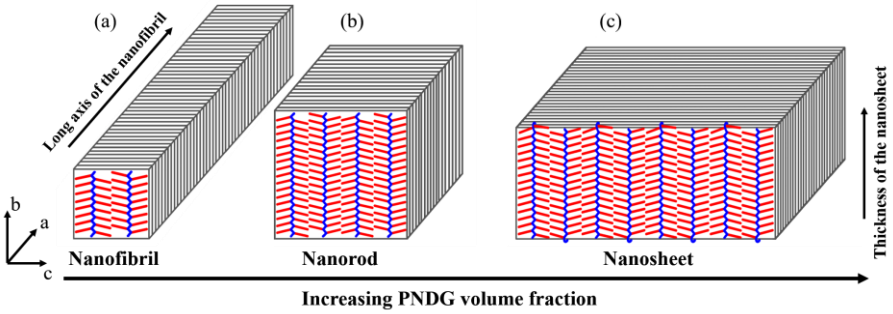

Figure 3. Schematic illustration of molecular packings of the core-forming PNDG blocks within (a) a nanofibril (PNMG$_{105}$-*b*-PNDG$_{20}$), (b) a nanorod (PNMG$_{121}$-*b*-PNDG$_{46}$) and (c) a nanosheet (PNMG$_{124}$-*b*-PNDG$_{63}$), respectively. The backbones and *n*-decyl side chains of PNDG are indicated in blue and red, respectively. The solvophilic PNMG segments connected to the chain end of PNDG backbone is omitted for clarity.

Based on the model fitting results (Table 1), the average cross-sectional area of the PNDG core inside of the PNMG$_{105}$-*b*-PNDG$_{20}$ nanofibrils is found to be 34.2 nm^2. The facial area of the PNDG$_{20}$ segment, *i.e.*, the surface area of the fully extended PNDG$_{20}$ segment with all *cis*-amide conformation along crystallographic b and c axes (Figure S1), is estimated to be 14.4 nm^2.[51] Thus, the cross section of the nanofibril core should have at least two side-by-side stacked PNDG molecules (Figure 3(a) and $N_{\text{agg, cross}}$ in Table 1).

Effect of Polymer Composition on the Structure and Morphology of Coil-Comb Shaped Diblock Copolypeptoid Micelles. As crystallization of the core-forming PNDG segments play an important role in the morphology of the coil-comb shaped block copolypeptoids in solution, we further investigated how increasing the chain length (or the volume fraction) of the PNDG segments influences the morphology of nanostructures formed by CDSA. Figure 4(a) shows the morphology of the self-assembled PNMG$_{121}$-*b*-PNDG$_{46}$ nanostructures in dilute methanol. Unlike the long worm-like

nanofibrils formed by CDSA of PNMG$_{105}$-*b*-PNDG$_{20}$ (f_{PNDG} = 0.44), the PNMG$_{121}$-*b*-PNDG$_{46}$ having an intermediate PNDG volume fraction (f_{PNDG} = 0.61, Table 1) self-assembled into rigid rod-like structures with much shorter length in methanol. The average length of the nanorods estimated from cryo-TEM are in a range of approximately 100 - 400 nm. As the PNMG$_{121}$-*b*-PNDG$_{46}$ nanorods are much shorter in length relative to PNMG$_{105}$-*b*-PNDG$_{20}$ nanofibrils with micron lengths (Figure 1(a)), the 2D scattering pattern of the former is nearly isotropic under unidirectional flow in the capillary tube. Thus, all X-ray results of the PNMG$_{121}$-*b*-PNDG$_{46}$ nanorods discussed below were collected under static condition without flow.

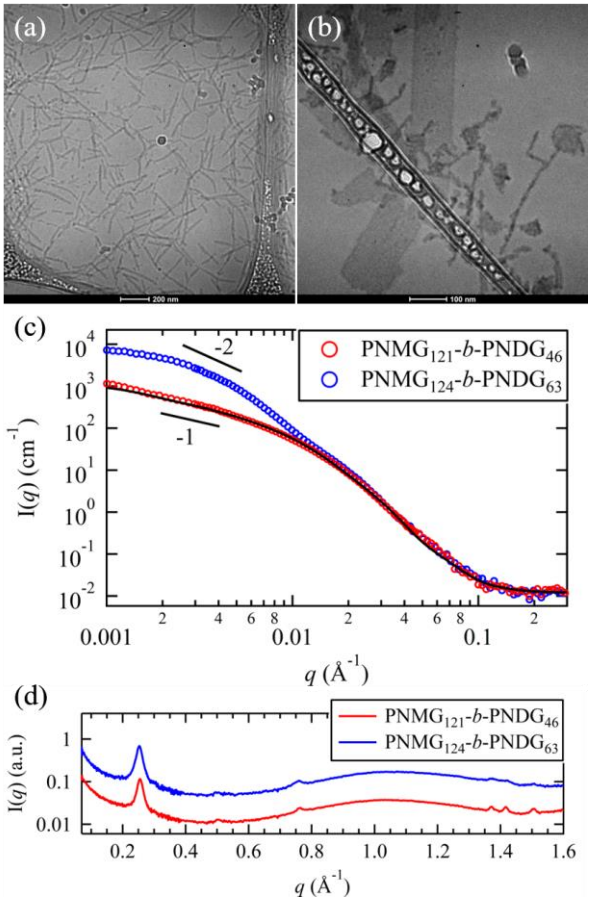

Figure 4. Representative cryo-TEM images for (a) PNMG$_{121}$-*b*-PNDG$_{46}$ and (b) PNMG$_{124}$-*b*-PNDG$_{63}$ in diluted methanol solutions (1 mg/ml). (c) SANS intensity profile (open circles) for the 5 mg/ml PNMG$_{121}$-*b*-PNDG$_{46}$ and PNMG$_{124}$-*b*-PNDG$_{63}$ in deuterated methanol measured at a static state. The solid line in (c) corresponds to the best-fit to the data based on the cylindrical micelle model described in the text. (d) MAXS/WAXS intensity profiles for the 5 mg/ml PNMG$_{121}$-*b*-PNDG$_{46}$ and PNMG$_{124}$-*b*-PNDG$_{63}$ in methanol measured at a static state.

The SANS data of PNMG$_{121}$-*b*-PNDG$_{46}$ nanorods (Figure 4(c)) can be well-fitted using the same cylindrical micelle model as described earlier, affording a PNDG core radius of R_c = 6.8 ± 0.2 nm and a polydispersity of R_c of 0.3. The average diameter of the PNMG$_{121}$-*b*-PNDG$_{46}$ nanorods obtained by SANS analysis is approximately 38.0 nm, which is larger than that (27 nm) determined by the cryo-TEM imaging. The discrepancy is likely due to the diminished contrast of the corona regions of nanorods against the solvent background under

cryo-TEM (Figure S12). The detailed structural parameters of nanorods obtained by the SANS analysis were summarized in Table 1. The $PNMG_{121}$-*b*-$PNDG_{46}$ nanorods were found to have much thicker PNDG core comparing to the $PNMG_{105}$-*b*-$PNDG_{20}$ nanofibrils. The corresponding M/WAXS results (Figure 4(d)) show discrete reflection peaks due to the crystalline PNDG domains at nearly identical *q* positions to those observed for the $PNMG_{105}$-*b*-$PNDG_{20}$ nanofibrils, suggesting that the crystalline packing in the core of $PNMG_{121}$-*b*-$PNDG_{46}$ nanorods are very similar to that in the $PNMG_{105}$-*b*-$PNDG_{20}$ nanofibrils. Assuming the crystalline packing of the PNDG segments in the $PNMG_{121}$-*b*-$PNDG_{46}$ nanorods are identical to that in the $PNMG_{105}$-*b*-$PNDG_{20}$ nanofibrils, the cross section of the former core would have at least 4 $PNDG_{46}$ molecules stacked side-by-side in a fully extended *cis*-amide backbone conformation. (Note: the facial area of a fully extended all-*cis* $PNDG_{46}$ block is estimated to be 33.1 nm^2) (Figure 3(b) and $N_{agg,\ cross}$ in Table 1).

As the volume fraction of PNDG segments is further increased to 0.68 such as in the sample of $PNMG_{124}$-*b*-$PNDG_{63}$, cryo-TEM analysis of their dilute methanol solution revealed the predominant presence of two-dimensional (2D) nanosheets in addition to some short nanorods (Figure 4(b) and Figure S13). The SANS profile of the $PNMG_{124}$-*b*-$PNDG_{63}$ solution exhibits elevated intensity in the low *q* range and a $I \sim q^{-2}$ dependence near $q \sim 0.0035$ $Å^{-1}$ as compared to a $I \sim q^{-1}$ dependence for the $PNMG_{121}$-*b*-$PNDG_{46}$ solution (Figure 4 (c)), consistent with the formation of 2D lamellae-like structures for the former and 1D rod-like structures for the latter. In addition, the majority of the nanosheets exhibit a rectangular shape that is ~ 100 nm in width and several hundreds of nanometers in length. The average thickness of the $PNMG_{124}$-*b*-$PNDG_{63}$ nanosheets was estimated to be ~ 14 nm based on atomic force microscopy (AFM) (Figure S14). M/WAXS analysis of $PNMG_{124}$-*b*-$PNDG_{63}$ nanosheets (Figure 4(d)) revealed notable scattering peaks due to the (001), (002) and (003) reflections,

indicating molecular ordering due to side-by-side packing PNDG segments along the crystallographic c-axis. By contrast, the (100) reflection and the associated higher order (101) and (102) reflections are barely discernible in the WAXS region, indicating the relatively poor molecular ordering of adjacent PNDG backbones along the crystallographic a-axis (Figure 3(c)). This result suggests that the formation of PNMG$_{124}$-*b*-PNDG$_{63}$ nanosheets is mainly driven by the molecular packing along the crystallographic c-axis, while the molecular packing along the a-axis is significantly diminished. Given that the PNDG backbone ends are linked with solvated PNMG chains and the PNDG crystals thus do not grow in the crystallographic b-axis, it is reasonable that the dimension of the nanosheet along b-axis corresponds to the thickness of the nanosheet, as shown in Figure 3(c). This molecular arrangement would also minimize the unfavorable interaction between the solvent and the relatively solvophobic PNDG sidechains. Based on the MAXS/WAXS results, we postulate that the length of the nanosheets are determined the side-by-side packing of PNDG segments along the crystallographic c-axis, whereas the width of the nanosheets is resulted from the face-to-face stacking of the PNDG segments (Figure 4(c)). This picture is consistent with recent cryo-electron microscopy and molecular dynamic simulation studies on crystallizable diblock copolypeptoid nanosheets.[66] In addition, we have found that the lattice constant of (001) plane, *i.e.*, the distance of adjacent PNDG backbones separated by the long *n*-decyl side chains, slightly increased to 2.5 nm for the PNMG$_{124}$-*b*-PNDG$_{63}$ nanosheets as compared to that of the PNMG-*b*-PNDG nanofibrils and nanorods with smaller PNDG volume fractions (2.4 nm). Meanwhile, the (001) peak is slightly broader (Figure S15). By fitting the primary peak to a Gaussian function, the full width at half-maximum (FWHM) of the (001) peak of PNMG$_{124}$-*b*-PNDG$_{63}$ is estimated to be 0.022 A^{-1}, which is larger than those obtained from PNMG$_{105}$-*b*-PNDG$_{20}$ nanofibrils (0.018 A^{-1}) and PNMG$_{121}$-*b*-PNDG$_{46}$ nanorods (0.014 A^{-1}). These imply that the molecular

packing of PNDG backbones along the crystallographic c-axis in the $PNMG_{124}$-*b*-$PNDG_{63}$ nanosheets is more disordered than those of the nanofibrils and nanorods.

The above results clearly shown that the structure and morphology of coil-comb shaped block copolypeptoids nanostructures are dependent on the volume fraction of the crystallizable PNDG segment relative to that of the PNMG segment. With relatively low PNDG volume fraction (0.44), the PNMG-*b*-PNDG molecules predominantly self-assemble into long worm-like nanofibrils in dilute methanol solution upon crystallization. With increasing volume fraction of the PNDG block (0.61-0.68), the final morphology of the PNMG-*b*-PNDG nanostructures changes into short nanorods and then to nanosheets.

Investigation of Self-Assembly Pathways for Coil-Comb Shaped Block Copolypeptoids in Dilute Solution. Self-assembly pathways are important for the morphology of block copolymer solutions.[9, 32] To gain insights regarding the mechanism for the formation $PNMG_{105}$-*b*-$PNDG_{20}$ nanofibrils, we conducted time-dependent S/M/WAXS experiments on the $PNMG_{105}$-*b*-$PNDG_{20}$ methanol solution (5 mg/mL) at room temperature after being cooled down from 65 °C within in ~ 6 min. First, it should be mentioned that the SAXS profile of $PNMG_{105}$-*b*-$PNDG_{20}$ methanol solution at 65 °C shows relatively weak scattering and a flat Guinier regime at low q with no intensity upturn (Figure S16(a)). The Guinier analysis of the SAXS data at 65 °C (Figure S16(b)) gives a radius of gyration (R_g) of 2.3 nm, corresponding to the size of a single $PNMG_{105}$-*b*-$PNDG_{20}$ chain (*i.e.*, unimer) in methanol. This indicates that $PNMG_{105}$-*b*-$PNDG_{20}$ polymers are well-dissolved and exist as unimers in 65 °C methanol at 5 mg/mL concentration.

Upon cooling the solution to room temperature, a drastic change of the scattering profile was observed (Figure 5). At time t = 0 min, *i.e.*, immediately after the solution was cooled down from 65°C

to room temperature, the SAXS profile shows a noticeable upturn at the low q region, while the overall intensity is still relatively weak. Such intensity upturn with a $q^{-2.5}$ dependence is attributed to the formation of polymer aggregates, *i.e.*, the "seeds", at the very early stage after the solution was cooled down to room temperature. With increasing of time, as shown in Figure 5(b), multiple peaks attributed to the crystalline packing of PNDG segments along the crystallographic a and c axes, *i.e.*, the (001), (100) and their higher order reflections, started to appear after ~100 min and intensify over time in the M/WAXS profiles. Meanwhile, at the low q regime in SAXS spectra, the dependence of intensity over q gradually changed over from I ~ $q^{-2.5}$ to $q^{-1.5}$, and eventually to q^{-1} after ~ 400 min, while the overall absolute SAXS intensity continue to increase until a final state was reached. We attribute this increase in the SAXS intensity mainly due to the one-dimensional elongation of the nanofibrils, consistent with the previous observation by the time-dependent cryo-TEM.[44] In addition , S/MAXS profiles of the PNMG$_{105}$-*b*-PNDG$_{20}$ methanol solution (5 mg/mL) at ~15 day and

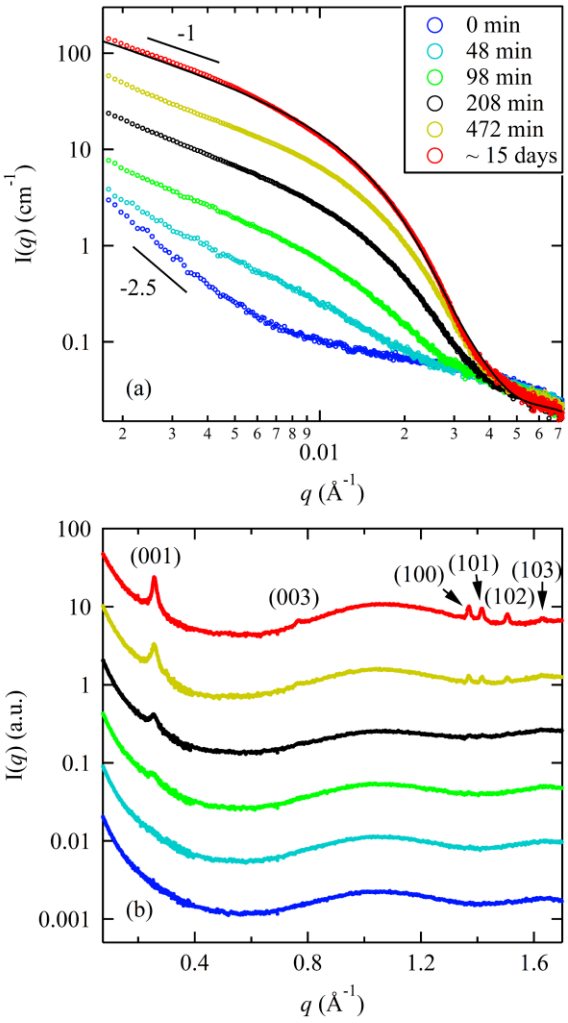

Figure 5. (a) SAXS profiles of 5 mg/mL PNMG$_{105}$-*b*-PNDG$_{20}$ methanol solution at different waiting time (t). The corresponding MAXS/WAXS profiles in the high q regime were plotted in (b), in which the intensity data at different times have been shifted vertically by multiplying the MAXS/WAXS intensity by a factor of 5 for clarity. The solid line in (a) corresponds to the best-fit to the final equilibrium SAXS result based on the cylindrical micelle model described in the text.

3 month are identical (Figure S17), indicating that 15 days is sufficient for the formation of the fibrils to reach a final state.[44] As illustrated earlier in Figure 3(a), we conclude that the elongation of $PNMG_{105}$-*b*-$PNDG_{20}$ nanofibrils is induced by the face-to-face packing of PNDG backbones along the crystallographic a-axis (*i.e.*, the (100) packing), while the thickness (or lateral diameter) of the nanofibrils is determined by both the backbone length (or b dimension) of PNDG and the (001) packing along the crystallographic c-axis.

Although the scattering peaks corresponds to the (001) and (100) peaks are only weakly present from the MAXS/WAXS profile due to low concentration of crystalline fragments at the initial stage (*i.e.*, ~ 1 hour), it is likely that the initial seed crystals also involve the molecular packing along both crystallographic a and c axes. In addition, the unimer addition to the micelles do not occur equally in in all crystallographic directions. As we have observed for the $PNMG_{105}$-*b*-$PNDG_{20}$ nanofibrils, the face-to-face stacking of PNDG segment along the crystallographic a-axis is favored over the side-by-side packing along the c-axis during the seeded growth process, resulting in long worm-like micelles.

As a result, we concluded that the slow formation of the $PNMG_{105}$-*b*-$PNDG_{20}$ nanofibrils is mainly governed by the so-called "self-seeding growth" mechanism (Figure 6).[5, 13, 18, 20, 27, 67, 68] Driven by the crystallization of the PNDG segments, the homogeneous/self-nucleation of $PNMG_{105}$-*b*-$PNDG_{20}$ unimers in solution creates initial "seed" micellar fragments upon cooling the solution to room temperature.[5, 6, 18, 20, 27] These seed crystals serve as "initiators" for subsequent deposition of soluble unimers at the crystalline front, facilitating the steady growth of nanofibrils until all unimers are consumed. Thus, that the average length of the final nanofibrils is expected to be correlated to the relative initial seeds versus the unimer concentration, *i.e.*, higher initial seeds concentration would result in shorter nanofibrils and *vice versa*. The nature and extent of initial seed crystal formation is

dependent on the cooling profile and solution concentration, if there were to be formed *in situ*. One can envision the control of average length of nanofibrils by adding exogenously generated seed crystals to a PNMG$_{105}$-*b*-PNDG$_{20}$ unimer solution of known concentration, as has been demonstrated in the living CDSA of polyferrocenylsilane [4, 7, 14, 20, 25, 27, 28] or polylactide-containing block copolymers in solution.[16] This aspect will be investigated in our future efforts.

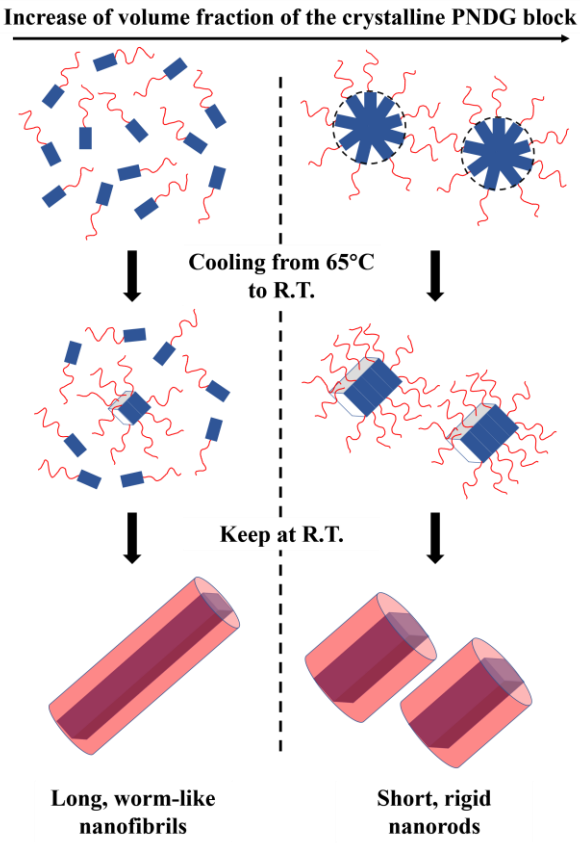

Figure 6. Schematic illustration of the proposed self-assembly mechanisms for nanofibrils (PNMG$_{105}$-*b*-PNDG$_{20}$) (left) and nanorods (PNMG$_{121}$-*b*-PNDG$_{46}$) (right) with different PNDG volume fractions via crystallization-driven self-assembly (CDSA) in methanol. The PNMG and PNDG blocks are indicated in red and blue, respectively.

In contrast to the self-seeding growth mechanism for the PNMG$_{105}$-*b*-PNDG$_{20}$ nanofibrils, the formation of PNMG$_{121}$-*b*-PNDG$_{46}$ nanorods was found to occur by a very different self-assembly pathway. First of all, S/MAXS analysis of the PNMG$_{121}$-*b*-PNDG$_{46}$ methanol solution (5 mg/mL) at 65 °C (Figure S16(a)) revealed the formation of amorphous spherical micelles with R_g = 14.9 nm (Figure S16(c)). This is in contrast to the PNMG$_{105}$-*b*-PNDG$_{20}$ methanol solution in which all polymers exist as unimers (R_g = 2.3 nm) at 65 °C. The association of PNMG$_{121}$-*b*-PNDG$_{46}$ molecules into small aggregates at high temperature was also confirmed by cryo-TEM analysis (Figure S18). We attributed the large difference in the initial association state at high temperature (*i.e.*, above the crystallization temperature of PNDG) to the solubility difference of these polymers in methanol, which is mainly governed by their relative volume

fraction of the solvophobic PNDG segments. In addition, no crystallization was observed for either solution sample at 65 °C (Figure S16(d)).

The PNMG$_{121}$-*b*-PNDG$_{46}$ solution was then cooled down to room temperature from 65 °C with a similar cooling rate as that for the PNMG$_{105}$-*b*-PNDG$_{20}$ solution. In contrast to the notable change in the SAXS profiles of the PNMG$_{105}$-*b*-PNDG$_{20}$ sample as a function of time (Figure 5(a)), the SAXS profiles of the PNMG$_{121}$-*b*-PNDG$_{46}$ solution did not change significantly in both shape and intensity over time at room temperature (Figure 7(a)). Interestingly, the simultaneously collected MAXS analysis revealed the presence of well-defined (001) reflection peak immediately upon cooling the solution to room temperature (Figure 7(b) and S16(e)) and a steady intensity increase over time, indicating the rapid formation of crystalline domains in the solution. It is clear that crystallization has already started during the cooling process. If we consider the length of the PNMG$_{121}$-*b*-PNDG$_{46}$ nanorods to be ~ 200 nm at the final state (as estimated from the cryo-TEM images (Figure 4(a)), the aggregation number of the PNMG$_{121}$-*b*-PNDG$_{46}$ nanorods will be ~ 1834 with a core cross-section radius R_c = 6.8 ± 0.2 nm. This is about 10 times larger than that of the amorphous spherical micelle precursor (~ 175) at 65 °C prior to the onset of crystallization (Figure S19 and Table S1). This clearly indicates that the fusion and structural re-arrangement of preformed spherical micelles must have occurred to yield the

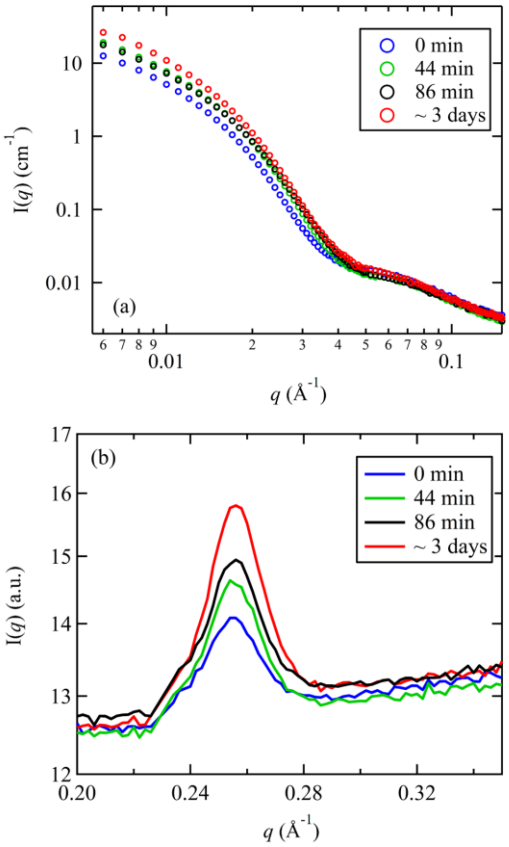

Figure 7. (a) SAXS and (b) normalized MAXS intensity profiles (near q = 0.26 Å^{-1}) of 5 mg/mL PNMG$_{121}$-*b*-PNDG$_{46}$ methanol solution at different waiting time (t) after the solution was cooled to 20 °C.

final nanorods.

It is evident that the self-assembly pathway for the $PNMG_{121}$-*b*-$PNDG_{46}$ nanorods is distinctly different from the self-seeding growth for the $PNMG_{105}$-*b*-$PNDG_{20}$ nanofibril formation, as depicted in Figure 6. For the $PNMG_{105}$-*b*-$PNDG_{20}$ solution, the polymer existed as individual unimers at high temperature. Cooling the solution down to room temperature (*i.e.*, below the crystallization temperature of PNDG) induces the nucleation of few seed crystals with crystallized PNDG segments in solution. The remaining PNMG-*b*-PNDG free chains present in relatively high concentration are continuously deposited onto the crystalline front of the seeds until all the free unimers are consumed, resulting in the gradual formation of long worm-like nanofibrils having anisotropic crystalline core in the solution. By contrast, in the $PNMG_{121}$-*b*-$PNDG_{46}$ solution, spherical micelles with an amorphous PNDG core formed initially at high temperature, which is presumably favored due to reduced solubility of the $PNMG_{121}$-*b*-$PNDG_{46}$ with higher PNDG content. In addition, the concentration of free $PNMG_{121}$-*b*-$PNDG_{46}$ unimers is expected to be very limited due to the micelle formation at 65 °C. As dissociation of micelles upon cooling to room temperature is highly unlikely, we can conclude that the pre-formed spherical micelles of $PNMG_{121}$-*b*-$PNDG_{46}$ must undergo confined crystallization of PNDG within the micellar core upon cooling,[8,9] and subsequently form elongated rod-like nanostructure by crystallization-induced fusion of the micelles.

The formation mechanism becomes more complex for the $PNMG_{124}$-*b*-$PNDG_{63}$ nanosheets and is not fully understood. The high-temperature SAXS result for the $PNMG_{124}$-*b*-$PNDG_{63}$ solution revealed a sharp intensity upturn with a q^{-3} dependence at low-*q*, indicating the possible formation of large aggregates at 65 °C before the onset of crystallization at low temperature (20°C) (Figure S20). The formation of large aggregates at 65 °C has also been confirmed by cryo-TEM analysis (Figure

S21). These results clearly suggest polymer association prior to onset of crystallization en route towards the nanosheets. However, it is presently unclear how crystallization of PNDG upon cooling plays a role in the final formation of nanosheet morphology.

Regarding the crystalline packing of PNDG chains within the nanosheets, the molecular ordering along the a-axis is significantly diminished relative to that along the c-axis, as evidenced by the weakened (100) peak and its higher order peaks relative to the (001) peak shown in Figure 4 (d) and Figure S15. This is in contrast to an earlier study of the 2D nanosheets formed by crystalline-coil peptoid diblock oligomers in which the face-to-face stacking of peptoid oligomer chains along the (100) direction is favored.[54] We propose that the possible intramolecular folding of long polypeptoid backbones and the difference in the intermolecular interactions among the side chains may have contributed to this discrepancy. For polypeptoid molecules with long and linear aliphatic side chains, such as PNDG, the *cis*-amide backbones are more likely to fold along the crystallographic a-axis rather than c-axis, due to steric hindrance of aliphatic side chains. As a result, the molecular packing of the folded long PNDG blocks (*i.e.*, $PNDG_{63}$) along a-axis is likely to be more disordered relative to that of unfolded short chains. In addition, the nature of side chains also influences the propensity of face-to-face stacking relative to the side-by-side stacking of peptoid chains. As compared to linear aliphatic side chains, aromatic side chains can promote the face-to-face packing through π-π interactions. Further studies on the effects of chain folding and side chain chemistry of comb-shaped polypeptoids on solution aggregate structure will be pursued in future.

CONCLUSIONS

CDSA of coil-comb shaped diblock copolypeptoids, *i.e.*, PNMG-*b*-PNDGs, in dilute methanol solutions has been investigated using X-ray/neutron scattering and cryo-TEM techniques. It was found

that as the chain length and volume fraction of crystallizable PNDG segments increases, the dilute solution morphology of PNMG-*b*-PNDG diblock copolymers can be tailored from 1D worm-like nanofibrils to 1D rigid nanorods and then 2D nanosheets. While all nanostructures consist of a crystalline PNDG core, their self-assembly pathways can be distinctly different under identical conditions. A self-seeding growth mechanism which is shown to be operative for the formation of nanofibrils involves the initial formation of a few small "seed" crystals followed by the preferential addition of the unimers to a certain crystallographic facet of the PNDG crystalline core, thus enabling unidirectional elongation of the molecular assemblies with an anisotropic crystalline core. This is rendered possible by the relatively low PNDG content in the block copolypeptoids, resulting in good solubility of the block copolymers at high temperature prior to onset of CDSA. By contrast, for diblock copolypeptoids with relatively high PNDG contents, their reduced solubility resulted in complex initial associated states prior to onset of CDSA. In this case, their solution self-assembly can proceed by a two-stage process involving the initial formation of amorphous spherical micelles followed by the crystallization-driven fusion and reorganization of the micelles to form short nanorods with a crystalline core. These findings have highlighted the important role of self-assembly pathways on the solution morphology of coil-crystalline block copolymers. Considering the combination of desirable properties of polypeptoids, CDSA of coil-comb shaped block copolypeptoids can be used for the further development of new biomaterials and bio-devices with tunable polymer structures and functionalities. Detailed investigations on the role of polymer molecular weight, chemical composition, polymer concentration, crystallization temperature and solvent quality are in progress for a more comprehensive understanding of the self-assembly of coil-comb shaped diblock copolypeptoids in

solution. Future work will also be focused on investigating how to control the CDSA processes to access 1D and 2D polypeptoid nanostructures with tailorable dimension and composition in high yields.

CONFLICTS OF INTEREST

The authors declare no competing financial interest.

ASSOCIATED CONTENT

Supporting Information

Materials and Methods, general crystalline packing of comb-like polypeptoids, ^{1}H NMR spectra of the PNMG-*b*-PNDG block copolymers, SEC-DRI chromatograms of the PNMG-*b*-PNDG block copolymers, additional TEM/cryo-TEM images for the nanofibrils, nanorods and nanosheets, static liquid contact angle of the PNDG film, size distributions of rod-like core cross-sectional radius, 2D SAXS/WAXS/MAXS images at static state and at different flow rates, schematic experimental setup for X-ray solution scattering under flow, AFM results for the nanorods and nanosheets, a comparison of MAXS/WAXS profiles among different nanostructures, additional SAXS/MAXS results for PNMG-*b*-PNDGs, model fitting and fitting parameters of the SAXS profile of $PNMG_{121}$-*b*-$PNDG_{46}$ sample measured at 65 °C.

The Supporting Information is available free of charge on the ACS Publications website http://www.acs.org

Present Address

[±]N.J.: School of Materials Science and Engineering, University of Science and Technology Beijing, Beijing 100083, China

ACKNOWLEDGMENT

The authors thank Dr. Steven J. Weigand, Dr. Lin Yang and Dr. Richard E. Gillilan for providing assistance in the synchrotron X-ray scattering measurements, Ms. Neepa M. K. Kuruppu Arachchige and Dr. Jayne C. Garno for assisting the AFM measurements, Dr. Jibao He for the cryo-TEM measurements, Ms. Liying Kang and Mr. Hongbiao Zhai for the additional TEM measurements. The polymer synthesis and characterization of polymer solution were supported by the National Science Foundation (CHE 1609447). The neutron scattering experiment was supported by the U.S. Department of Energy (DOE) under EPSCoR grant no. DE-SC0012432 with additional support from the Louisiana Board of Regents. The neutron scattering work also used resources at the High Flux Isotope Reactor, a U.S. DOE Office of Science User Facility operated by the Oak Ridge National Laboratory. The Bio-SANS of the Center for Structural Molecular Biology at the High Flux Isotope Reactor is supported by the Office of Biological and Environmental Research of the U.S. DOE. The X-ray scattering work was performed at the DuPont-Northwestern-Dow Collaborative Access Team (DND-CAT) of the Advanced Photon Source (APS). DND-CAT is supported by Northwestern University, E.I. DuPont de Nemours & Co., and The Dow Chemical Company. This research used resources of the Advanced Photon Source, a U.S. DOE Office of Science User Facility operated for the DOE Office of Science by Argonne National Laboratory under Contract No. DE-AC02-06CH11357. This research also used resources of the Life Science X-ray Scattering (LiX/16-ID) beamline operated by the National Synchrotron Light Source II at Brookhaven National Laboratory, which is supported by the U.S. DOE, Office of Science, Office of Basic Energy Sciences, under Contract No. DE-SC0012704. The LiX beamline is also part of the Life Science Biomedical Technology Research resource, primarily supported by the National Institute of Health, National Institute of General Medical Sciences under Grant P41 GM111244, and by the DOE Office of Biological and Environmental Research under Grant

KP1605010, with additional support from NIH Grant S10 OD012331. Additional X-ray work was conducted at the Cornell High Energy Synchrotron Source (CHESS), which is supported by the National Science Foundation and the National Institutes of Health/National Institute of General Medical Sciences under NSF award DMR-1829070.

References

1. Geng, Y.; Dalhaimer, P.; Cai, S.; Tsai, R.; Tewari, M.; Minko, T.; Discher, D. E., Shape effects of filaments versus spherical particles in flow and drug delivery. *Nat Nanotechnol* **2007,** *2*, 249-255.

2. Kim, Y.; Dalhaimer, P.; Christian, D. A.; Discher, D. E., Polymeric worm micelles as nano-carriers for drug delivery. *Nanotechnology* **2005,** *16* (7), S484-S491.

3. Hartgerink, J. D.; Beniash, E.; Stupp, S. I., Self-Assembly and Mineralization of Peptide-Amphiphile Nanofibers. *Science* **2001,** *294* (5547), 1684-1688.

4. Gilroy, J. B.; Gädt, T.; Whittell, G. R.; Chabanne, L.; Mitchels, J. M.; Richardson, R. M.; Winnik, M. A.; Manners, I., Monodisperse cylindrical micelles by crystallization-driven living self-assembly. *Nat. Chem.* **2010,** *2*, 566-570.

5. Tritschler, U.; Pearce, S.; Gwyther, J.; Whittell, G. R.; Manners, I., 50th Anniversary Perspective: Functional Nanoparticles from the Solution Self-Assembly of Block Copolymers. *Macromolecules* **2017,** *50* (9), 3439-3463.

6. Foster, J. C.; Varlas, S.; Couturaud, B.; Coe, Z.; O'Reilly, R. K., Getting into Shape: Reflections on a New Generation of Cylindrical Nanostructures' Self-Assembly Using Polymer Building Blocks. *J. Am. Chem. Soc.* **2019,** *141* (7), 2742-2753.

7. Tritschler, U.; Gwyther, J.; Harniman, R. L.; Whittell, G. R.; Winnik, M. A.; Manners, I., Toward

Uniform Nanofibers with a π-Conjugated Core: Optimizing the "Living" Crystallization-Driven Self-Assembly of Diblock Copolymers with a Poly(3-octylthiophene) Core-Forming Block. *Macromolecules* **2018,** *51* (14), 5101-5113.

8. Yin, L.; Lodge, T. P.; Hillmyer, M. A., A Stepwise "Micellization–Crystallization" Route to Oblate Ellipsoidal, Cylindrical, and Bilayer Micelles with Polyethylene Cores in Water. *Macromolecules* **2012,** *45* (23), 9460-9467.

9. Schmelz, J.; Karg, M.; Hellweg, T.; Schmalz, H., General Pathway toward Crystalline-Core Micelles with Tunable Morphology and Corona Segregation. *ACS Nano* **2011,** *5* (12), 9523-9534.

10. Li, Z.; Liu, R.; Mai, B.; Wang, W.; Wu, Q.; Liang, G.; Gao, H.; Zhu, F., Temperature-induced and crystallization-driven self-assembly of polyethylene-b-poly(ethylene oxide) in solution. *Polymer* **2013,** *54* (6), 1663-1670.

11. He, W.-N.; Zhou, B.; Xu, J.-T.; Du, B.-Y.; Fan, Z.-Q., Two Growth Modes of Semicrystalline Cylindrical Poly(ε-caprolactone)-b-poly(ethylene oxide) Micelles. *Macromolecules* **2012,** *45* (24), 9768-9778.

12. Rizis, G.; van de Ven, T. G. M.; Eisenberg, A., "Raft" Formation by Two-Dimensional Self-Assembly of Block Copolymer Rod Micelles in Aqueous Solution. *Angew. Chem. Int. Ed.* **2014,** *53* (34), 9000-9003.

13. Arno, M. C.; Inam, M.; Coe, Z.; Cambridge, G.; Macdougall, L. J.; Keogh, R.; Dove, A. P.; O'Reilly, R. K., Precision Epitaxy for Aqueous 1D and 2D Poly(ε-caprolactone) Assemblies. *J. Am. Chem. Soc.* **2017,** *139* (46), 16980-16985.

14. Petzetakis, N.; Dove, A. P.; O'Reilly, R. K., Cylindrical micelles from the living crystallization-

driven self-assembly of poly(lactide)-containing block copolymers. *Chem. Sci.* **2011,** *2* (5), 955-960.

15. Pitto-Barry, A.; Kirby, N.; Dove, A. P.; O'Reilly, R. K., Expanding the scope of the crystallization-driven self-assembly of polylactide-containing polymers. *Polym. Chem.* **2014,** *5* (4), 1427-1436.

16. Sun, L.; Petzetakis, N.; Pitto-Barry, A.; Schiller, T. L.; Kirby, N.; Keddie, D. J.; Boyd, B. J.; O'Reilly, R. K.; Dove, A. P., Tuning the Size of Cylindrical Micelles from Poly(l-lactide)-b-poly(acrylic acid) Diblock Copolymers Based on Crystallization-Driven Self-Assembly. *Macromolecules* **2013,** *46* (22), 9074-9082.

17. Inam, M.; Cambridge, G.; Pitto-Barry, A.; Laker, Z. P. L.; Wilson, N. R.; Mathers, R. T.; Dove, A. P.; O'Reilly, R. K., 1D vs. 2D shape selectivity in the crystallization-driven self-assembly of polylactide block copolymers. *Chem. Sci.* **2017,** *8* (6), 4223-4230.

18. Wang, X.; Guerin, G.; Wang, H.; Wang, Y.; Manners, I.; Winnik, M. A., Cylindrical Block Copolymer Micelles and Co-Micelles of Controlled Length and Architecture. *Science* **2007,** *317* (5838), 644-647.

19. Presa Soto, A.; Gilroy, J. B.; Winnik, M. A.; Manners, I., Pointed-Oval-Shaped Micelles from Crystalline-Coil Block Copolymers by Crystallization-Driven Living Self-Assembly. *Angew. Chem. Int. Ed.* **2010,** *49* (44), 8220-8223.

20. Qian, J.; Lu, Y.; Chia, A.; Zhang, M.; Rupar, P. A.; Gunari, N.; Walker, G. C.; Cambridge, G.; He, F.; Guerin, G.; Manners, I.; Winnik, M. A., Self-Seeding in One Dimension: A Route to Uniform Fiber-like Nanostructures from Block Copolymers with a Crystallizable Core-Forming Block. *ACS Nano* **2013,** *7* (5), 3754-3766.

21. Gilroy, J. B.; Rupar, P. A.; Whittell, G. R.; Chabanne, L.; Terrill, N. J.; Winnik, M. A.; Manners,

I.; Richardson, R. M., Probing the Structure of the Crystalline Core of Field-Aligned, Monodisperse, Cylindrical Polyisoprene-block-Polyferrocenylsilane Micelles in Solution Using Synchrotron Small- and Wide-Angle X-ray Scattering. *J. Am. Chem. Soc.* **2011,** *133* (42), 17056-17062.

22. Hsiao, M.-S.; Yusoff, S. F. M.; Winnik, M. A.; Manners, I., Crystallization-Driven Self-Assembly of Block Copolymers with a Short Crystallizable Core-Forming Segment: Controlling Micelle Morphology through the Influence of Molar Mass and Solvent Selectivity. *Macromolecules* **2014,** *47* (7), 2361-2372.

23. Hudson, Z. M.; Boott, C. E.; Robinson, M. E.; Rupar, P. A.; Winnik, M. A.; Manners, I., Tailored hierarchical micelle architectures using living crystallization-driven self-assembly in two dimensions. *Nat. Chem.* **2014,** *6*, 893.

24. Finnegan, J. R.; Lunn, D. J.; Gould, O. E. C.; Hudson, Z. M.; Whittell, G. R.; Winnik, M. A.; Manners, I., Gradient Crystallization-Driven Self-Assembly: Cylindrical Micelles with "Patchy" Segmented Coronas via the Coassembly of Linear and Brush Block Copolymers. *J. Am. Chem. Soc.* **2014,** *136* (39), 13835-13844.

25. Qiu, H.; Hudson, Z. M.; Winnik, M. A.; Manners, I., Multidimensional hierarchical self-assembly of amphiphilic cylindrical block comicelles. *Science* **2015,** *347* (6228), 1329-1332.

26. Qiu, H.; Gao, Y.; Du, V. A.; Harniman, R.; Winnik, M. A.; Manners, I., Branched Micelles by Living Crystallization-Driven Block Copolymer Self-Assembly under Kinetic Control. *J. Am. Chem. Soc.* **2015,** *137* (6), 2375-2385.

27. Qian, J.; Li, X.; Lunn, D. J.; Gwyther, J.; Hudson, Z. M.; Kynaston, E.; Rupar, P. A.; Winnik, M. A.; Manners, I., Uniform, High Aspect Ratio Fiber-like Micelles and Block Co-micelles with a Crystalline π-Conjugated Polythiophene Core by Self-Seeding. *J. Am. Chem. Soc.* **2014,** *136* (11),

4121-4124.

28. Patra, S. K.; Ahmed, R.; Whittell, G. R.; Lunn, D. J.; Dunphy, E. L.; Winnik, M. A.; Manners, I., Cylindrical Micelles of Controlled Length with a π-Conjugated Polythiophene Core via Crystallization-Driven Self-Assembly. *J. Am. Chem. Soc.* **2011,** *133* (23), 8842-8845.

29. Gilroy, J. B.; Lunn, D. J.; Patra, S. K.; Whittell, G. R.; Winnik, M. A.; Manners, I., Fiber-like Micelles via the Crystallization-Driven Solution Self-Assembly of Poly(3-hexylthiophene)-block-Poly(methyl methacrylate) Copolymers. *Macromolecules* **2012,** *45* (14), 5806-5815.

30. Moon, H. C.; Bae, D.; Kim, J. K., Self-Assembly of Poly(3-dodecylthiophene)-block-poly(methyl methacrylate) Copolymers Driven by Competition between Microphase Separation and Crystallization. *Macromolecules* **2012,** *45* (12), 5201-5207.

31. Gwyther, J.; Gilroy, J. B.; Rupar, P. A.; Lunn, D. J.; Kynaston, E.; Patra, S. K.; Whittell, G. R.; Winnik, M. A.; Manners, I., Dimensional Control of Block Copolymer Nanofibers with a π-Conjugated Core: Crystallization-Driven Solution Self-Assembly of Amphiphilic Poly(3-hexylthiophene)-b-poly(2-vinylpyridine). *Chem.: Eur. J* **2013,** *19* (28), 9186-9197.

32. Hayward, R. C.; Pochan, D. J., Tailored Assemblies of Block Copolymers in Solution: It Is All about the Process. *Macromolecules* **2010,** *43* (8), 3577-3584.

33. Nicolai, T.; Colombani, O.; Chassenieux, C., Dynamic polymeric micelles versus frozen nanoparticles formed by block copolymers. *Soft Matter* **2010,** *6* (14), 3111-3118.

34. Jain, S.; Bates, F. S., Consequences of Nonergodicity in Aqueous Binary PEO−PB Micellar Dispersions. *Macromolecules* **2004,** *37* (4), 1511-1523.

35. Lunn, D. J.; Finnegan, J. R.; Manners, I., Self-assembly of “patchy” nanoparticles: a versatile

approach to functional hierarchical materials. *Chem. Sci.* **2015,** *6* (7), 3663-3673.

36. Zhang, D.; Lahasky, S. H.; Guo, L.; Lee, C.-U.; Lavan, M., Polypeptoid Materials: Current Status and Future Perspectives. *Macromolecules* **2012,** *45* (15), 5833-5841.

37. Kirshenbaum, K.; Barron, A. E.; Goldsmith, R. A.; Armand, P.; Bradley, E. K.; Truong, K. T. V.; Dill, K. A.; Cohen, F. E.; Zuckermann, R. N., Sequence-specific polypeptoids: A diverse family of heteropolymers with stable secondary structure. *Proc. Natl. Acad. Sci. U.S.A.* **1998,** *95* (8), 4303-4308.

38. Sun, J.; Zuckermann, R. N., Peptoid Polymers: A Highly Designable Bioinspired Material. *ACS Nano* **2013,** *7* (6), 4715-4732.

39. Gangloff, N.; Ulbricht, J.; Lorson, T.; Schlaad, H.; Luxenhofer, R., Peptoids and Polypeptoids at the Frontier of Supra- and Macromolecular Engineering. *Chemical Reviews* **2016,** *116* (4), 1753-1802.

40. Lahasky, S. H.; Hu, X.; Zhang, D., Thermoresponsive Poly(α-peptoid)s: Tuning the Cloud Point Temperatures by Composition and Architecture. *ACS Macro Lett.* **2012,** *1* (5), 580-584.

41. Tao, X.; Deng, Y.; Shen, Z.; Ling, J., Controlled Polymerization of N-Substituted Glycine N-Thiocarboxyanhydrides Initiated by Rare Earth Borohydrides toward Hydrophilic and Hydrophobic Polypeptoids. *Macromolecules* **2014,** *47* (18), 6173-6180.

42. Zhu, L.; Simpson, J. M.; Xu, X.; He, H.; Zhang, D.; Yin, L., Cationic Polypeptoids with Optimized Molecular Characteristics toward Efficient Nonviral Gene Delivery. *ACS Appl. Mater. Inter.* **2017,** *9* (28), 23476-23486.

43. Guo, L.; Zhang, D., Cyclic Poly(α-peptoid)s and Their Block Copolymers from N-Heterocyclic Carbene-Mediated Ring-Opening Polymerizations of N-Substituted N-Carboxylanhydrides. *J. Am. Chem. Soc.* **2009,** *131* (50), 18072-18074.

44. Lee, C.-U.; Smart, T. P.; Guo, L.; Epps, T. H.; Zhang, D., Synthesis and Characterization of Amphiphilic Cyclic Diblock Copolypeptoids from N-Heterocyclic Carbene-Mediated Zwitterionic Polymerization of N-Substituted N-Carboxyanhydride. *Macromolecules* **2011,** *44* (24), 9574-9585.

45. Lee, C.-U.; Lu, L.; Chen, J.; Garno, J. C.; Zhang, D., Crystallization-Driven Thermoreversible Gelation of Coil-Crystalline Cyclic and Linear Diblock Copolypeptoids. *ACS Macro Lett.* **2013,** *2* (5), 436-440.

46. Lee, C.-U.; Li, A.; Ghale, K.; Zhang, D., Crystallization and Melting Behaviors of Cyclic and Linear Polypeptoids with Alkyl Side Chains. *Macromolecules* **2013,** *46* (20), 8213-8223.

47. Sun, J.; Teran, A. A.; Liao, X. X.; Balsara, N. P.; Zuckermann, R. N., Crystallization in Sequence-Defined Peptoid Diblock Copolymers Induced by Microphase Separation. *J. Am. Chem. Soc.* **2014,** *136* (5), 2070-2077.

48. Xuan, S.; Lee, C.-U.; Chen, C.; Doyle, A. B.; Zhang, Y.; Guo, L.; John, V. T.; Hayes, D.; Zhang, D., Thermoreversible and Injectable ABC Polypeptoid Hydrogels: Controlling the Hydrogel Properties through Molecular Design. *Chem. Mater.* **2016,** *28* (3), 727-737.

49. Sun, J.; Jiang, X.; Lund, R.; Downing, K. H.; Balsara, N. P.; Zuckermann, R. N., Self-assembly of crystalline nanotubes from monodisperse amphiphilic diblock copolypeptoid tiles. *Proc. Natl. Acad. Sci. U.S.A.* **2016,** *113* (15), 3954-3959.

50. Greer, D. R.; Stolberg, M. A.; Xuan, S.; Jiang, X.; Balsara, N. P.; Zuckermann, R. N., Liquid-Crystalline Phase Behavior in Polypeptoid Diblock Copolymers. *Macromolecules* **2018,** *51* (23), 9519-9525.

51. Greer, D. R.; Stolberg, M. A.; Kundu, J.; Spencer, R. K.; Pascal, T.; Prendergast, D.; Balsara, N.

P.; Zuckermann, R. N., Universal Relationship between Molecular Structure and Crystal Structure in Peptoid Polymers and Prevalence of the cis Backbone Conformation. *J. Am. Chem. Soc.* **2018,** *140* (2), 827–833.

52. Shi, Z.; Wei, Y.; Zhu, C.; Sun, J.; Li, Z., Crystallization-Driven Two-Dimensional Nanosheet from Hierarchical Self-Assembly of Polypeptoid-Based Diblock Copolymers. *Macromolecules* **2018,** *51* (16), 6344-6351.

53. Wei, Y.; Tian, J.; Zhang, Z.; Zhu, C.; Sun, J.; Li, Z., Supramolecular Nanosheets Assembled from Poly(ethylene glycol)-b-poly(N-(2-phenylethyl)glycine) Diblock Copolymer Containing Crystallizable Hydrophobic Polypeptoid: Crystallization Driven Assembly Transition from Filaments to Nanosheets. *Macromolecules* **2019,** *52* (4), 1546-1556.

54. Jin, H.; Jiao, F.; Daily, M. D.; Chen, Y.; Yan, F.; Ding, Y.-H.; Zhang, X.; Robertson, E. J.; Baer, M. D.; Chen, C.-L. Highly stable and self-repairing membrane-mimetic 2d nanomaterials assembled from lipid-like peptoids. *Nat. Commun.* **2016,** 7, 12252.

55. Birke, A.; Ling, J.; Barz, M., Polysarcosine-containing copolymers: Synthesis, characterization, self-assembly, and applications. *Prog. Polym. Sci.* **2018,** *81*, 163-208.

56. Fetsch, C.; Luxenhofer, R., Thermal Properties of Aliphatic Polypeptoids. *Polymers* **2013,** *5* (1), 112-127.

57. Rosales, A. M.; Murnen, H. K.; Zuckermann, R. N.; Segalman, R. A., Control of Crystallization and Melting Behavior in Sequence Specific Polypeptoids. *Macromolecules* **2010,** *43* (13), 5627-5636.

58. Edison, J. R.; Spencer, R. K.; Butterfoss, G. L.; Hudson, B. C.; Hochbaum, A. I.; Paravastu, A. K.; Zuckermann, R. N.; Whitelam, S., Conformations of peptoids in nanosheets result from the

interplay of backbone energetics and intermolecular interactions. *Proc. Natl. Acad. Sci. U.S.A.* **2018,** *115* (22), 5647-5651.

59. Pedersen, J. S.; Gerstenberg, M. C., Scattering Form Factor of Block Copolymer Micelles. *Macromolecules* **1996,** *29* (4), 1363-1365.

60. Pedersen, J. S., Form factors of block copolymer micelles with spherical, ellipsoidal and cylindrical cores. *J. Appl. Crystallogr.* **2000,** *33* (3-1), 637-640.

61. Lau, K. H. A.; Ren, C.; Sileika, T. S.; Park, S. H.; Szleifer, I.; Messersmith, P. B., Surface-Grafted Polysarcosine as a Peptoid Antifouling Polymer Brush. *Langmuir* **2012,** *28* (46), 16099-16107.

62. Hamley, I. W.; Burholt, S.; Hutchinson, J.; Castelletto, V.; da Silva, E. R.; Alves, W.; Gutfreund, P.; Porcar, L.; Dattani, R.; Hermida-Merino, D.; Newby, G.; Reza, M.; Ruokolainen, J.; Stasiak, J., Shear Alignment of Bola-Amphiphilic Arginine-Coated Peptide Nanotubes. *Biomacromolecules* **2017,** *18* (1), 141-149.

63. Trebbin, M.; Steinhauser, D.; Perlich, J.; Buffet, A.; Roth, S. V.; Zimmermann, W.; Thiele, J.; Förster, S., Anisotropic particles align perpendicular to the flow direction in narrow microchannels. *Proc. Natl. Acad. Sci. U.S.A.* **2013,** *110* (17), 6706-6711.

64. Yan, C.; Altunbas, A.; Yucel, T.; Nagarkar, R. P.; Schneider, J. P.; Pochan, D. J., Injectable solid hydrogel: mechanism of shear-thinning and immediate recovery of injectable β-hairpin peptide hydrogels. *Soft Matter* **2010,** *6* (20), 5143-5156.

65. Butler, P., Shear induced structures and transformations in complex fluids. *Curr. Opin. Colloid Interface Sci.* **1999,** *4* (3), 214-221.

66. Jiang, X.; Greer, D. R.; Kundu, J.; Ophus, C.; Minor, A. M.; Prendergast, D.; Zuckermann, R. N.;

Balsara, N. P.; Downing, K. H., Imaging Unstained Synthetic Polymer Crystals and Defects on Atomic Length Scales Using Cryogenic Electron Microscopy. *Macromolecules* **2018,** *51* (19), 7794-7799.

67. Xu, J.; Ma, Y.; Hu, W.; Rehahn, M.; Reiter, G., Cloning polymer single crystals through self-seeding. *Nat. Mater.* **2009,** *8* (4), 348-353.

68. Qian, J.; Guerin, G.; Lu, Y.; Cambridge, G.; Manners, I.; Winnik, M. A., Self-Seeding in One Dimension: An Approach To Control the Length of Fiberlike Polyisoprene–Polyferrocenylsilane Block Copolymer Micelles. *Angew. Chem. Int. Ed.* **2011,** *50* (7), 1622-1625.